Glial response to hypoxia in *trachealess* mutants induces synapse remodeling

Pei-Yi Chen[1,2], Yi-Wei Tsai[2], Angela Giangrande[3,4,5,6], and Cheng-Ting Chien[1,2,*]

[1]Institute of Neuroscience, National Yang-Ming University, Taipei, Taiwan

[2]Institute of Molecular Biology, Academia Sinica, Taipei, Taiwan

[3]Institut de Génétique et de Biologie Moléculaire et Cellulaire, Illkirch, France

[4]Centre National de la Recherche Scientifique, UMR7104, Illkirch, France

[5]Institut National de la Santé et de la Recherche Médicale, U964, Illkirch, France

[6]Université de Strasbourg, Illkirch, France

*Corresponding author: ctchien@gate.sinica.edu.tw (CTC)

Abstract

Synaptic structure and activity are sensitive to environmental alterations. Modulation of synaptic morphology and function is often induced by signals from glia. However, the process by which glia mediate synaptic responses to environmental perturbations such as hypoxia remains unknown. Here, we report that, in the *Drosophila trachealess* (*trh*) mutant, smaller synaptic boutons form clusters named bunch boutons appear at larval neuromuscular junctions (NMJs), which is induced by the reduction of internal oxygen levels due to defective tracheal branches. Thus, the bunch bouton phenotype in the *trh* mutant is suppressed by hyperoxia, and recapitulated in wild-type larvae raised under hypoxia. We further show that hypoxia-inducible factor (HIF)-1α/Similar (Sima) is critical in mediating hypoxia-induced bunch bouton formation. Sima upregulates the level of the Wnt/Wingless (Wg) signal in glia, leading to reorganized microtubule structures within presynaptic sites. Finally, hypoxia-induced bunch boutons maintain normal synaptic transmission at the NMJs, which is crucial for coordinated larval locomotion.

Author summary

Oxygen is essential for animals to maintain their life such as growth, metabolism, responsiveness, and movement. It is therefore important to understand how animal cells trigger hypoxia response and adapt to hypoxia thereafter. Both mammalian vascular and insect tracheal branches are induced to enhance the oxygen delivery. However, the study of hypoxia response in the nervous system remains limited. In this study, we assess the morphology of *Drosophila* neuromuscular junctions (NMJs), a model system to study development and function of synapses, in two hypoxia conditions, one with raising wild-type larvae in hypoxia, and the other in the *trachealess* (*trh*) mutant in which the trachea is defective, causing insufficient oxygen supply. Interestingly, glia, normally wrapping the axons of NMJs, invade into synapse and trigger Wg signals to reconstitute the synaptic structure under hypoxia. This synaptic remodeling maintains the synaptic transmission of synapse, which associate the locomotor behavior of larvae.

Introduction

Animals need oxygen and food, not only to sustain life, but also for motility. In vertebrates, oxygen and nutrients are delivered through the vascular systems to organs and tissues throughout the body. To maintain proper nutrient and oxygen supply, and thus physiological functions, the vascular system is also highly coordinated with the nervous system during development. Indeed, the vascular and nervous systems resemble each other in terms of their anatomical structures and developmental processes [1, 2]. In the brain, nerves and vessels, form close associations and are in physical contact through the third player astrocytes to form neurovascular units (NVU) [3]. Such organization is essential for controlling oxygen and glucose delivery through the blood vessels by neuronal activity, and this regulatory process is mediated through the coupled astrocytes [4]. However, some invertebrates lack the complex vascular systems [5]. In nematodes, oxygen is supplied simply by ambient diffusion to inner cells [6]. Insects such as *Drosophila* have evolved a prototype of the tracheal system to deliver oxygen and a primitive vascular system, the dorsal vessel, to facilitate nutrient delivery [7]. However, the physical association of nerves, trachea, and glial processes has also been demonstrated at the NMJs of adult *Drosophila* flight muscles [8].

Animals respond to changing oxygen levels by altering their oxygen delivery system. Insufficient oxygen levels (hypoxia) activate a broad range of genes to re-establish body homeostasis. One crucial regulator of these hypoxia-responsive genes is the sequence-specific DNA-binding transcription factor hypoxia inducible factor 1 (HIF-1) [9]. HIF-1 consists of α and β subunits that form heterodimers [10]. Whereas HIF-1β is expressed constitutively, HIF-1α protein levels are modulated by oxygen levels [11]. Under normal oxygen conditions (normoxia), oxygen-dependent prolyl

hydroxylases (PHDs) catalyze hydroxylation of a conserved prolyl residue in the central oxygen-dependent degradation (ODD) domain of HIF-1α [12-14]. Hydroxylation of HIF-1α promotes interaction with Von Hippel Lindau (VHL), which is the substrate recognition subunit of the cullin2-based E3 ubiquitin ligase, leading to HIF-1α ubiquitination and proteasomal degradation [15]. Under hypoxia, prolyl hydroxylation does not occur, HIF-1α proteins are stabilized and are translocated from the cytoplasm to the nucleus where they form heterodimers with HIF-1β to activate transcription of target genes [16, 17]. One major class of target genes encoding the Fibroblast Growth Factor (FGF) is involved in inducing angiogenesis in mammals. In *Drosophila,* the FGF member encoded by *Branchless* (*Bnl*) induces tracheal branching [18]. When oxygen levels are reduced, oxygen-starved cells express Bnl as a chemo-attractant to guide the growth tracheal terminal branches toward them [19].

In addition to adaptations of the respiratory system, the nervous system also responds to hypoxia. Oxygen levels modulate the survival, proliferation, and differentiation of radial glial cells (RGCs) in the human cerebral cortex. Interestingly, physiological hypoxia (3% O_2) induces neurogenesis and differentiation of RGCs into glutamatergic neurons [20]. Hypoxia induces neurite outgrowth in PC12 cells through activation of A2A receptor [21]. Brief exposure to anoxia and hypoglycemia caused axonal remodeling in hippocampal neurons, including presynaptic protrusion of filopodia and formation of multi-innervated spines [22]. Under hypoxia or upon depletion of PHD2, upregulation of the actin cross-linker Filamin A (FLNA) induces generation of more immature spines [23]. Astrocytes have been shown to play a crucial role in ischemic tolerance via the activation of P2X7 receptors, which trigger upregulation of HIF-1α [24].

93 Neuronal PAS (NPAS) proteins containing a DNA-binding Per-Arnt-Sim
94 domain function in vascular and nervous system development. In mice, NPAS1 is
95 responsible for cortical interneuron generation [25], whereas NPAS3 is required for
96 adult neurogenesis [26]. NPAS1 and NPAS3 also play key roles in lung development
97 [27, 28]. The homolog of NPAS1/3 in *Drosophila*, Trachealess (Trh), has been well
98 studied for its involvement in formation of the respiratory tracheal system. Trh is a
99 master regulator of tracheal cell fates, activating gene expression to induce tracheal
100 development [29, 30]. However, the role of Trh in the development of other tissues,
101 particularly the nervous system, is unknown. In this study, we found altered synaptic
102 bouton morphology at the NMJs of trh^1/trh^2 mutants. By performing *trh-RNAi*
103 knockdown and *UAS-trh* transgene rescue experiments, we show that *trh* is required
104 in tracheal cells for normal bouton formation. Defective tracheal branching in the
105 trh^1/trh^2 mutant mimics the effect of hypoxic conditions during larval development,
106 and supplying higher than normal oxygen levels restored normal bouton morphology.
107 We further show that glial cells respond to hypoxia by elevating Wnt/Wg expression
108 to mediate synaptic bouton remodeling through HIF1-α/Sima in *Drosophila*. Finally,
109 we reveal that this synaptic remodeling maintains normal synaptic transmission and it
110 is required for normal locomotion in larvae.

111 ## Results

112 ### *trh* modulates synaptic bouton formation non-cell autonomously

113 To understand the possible role of Trh in synapse formation, we examined
114 NMJ morphology in the *trh* mutants. Since both trh^1 *and* trh^2 loss-of-function alleles
115 are homozygous lethal [31-33], we examined the trans-heterozygous trh^1/trh^2 mutant
116 that survive to adult stages and compared it to wild-type (w^{1118}) and heterozygous
117 $trh^1/+$ controls. Synaptic boutons of w^{1118} and $trh^1/+$ NMJs were evenly spaced along
118 the axonal terminals, displaying the typical "beads-on-a-string" pattern (Fig 1A, upper
119 and middle panels, enlarged images at right). Strikingly, the trh^1/trh^2 mutant larvae
120 exhibited aberrant NMJ morphology in that their synaptic boutons were small and
121 formed clusters without discernable connections, particularly at the terminals (Fig 1A,
122 bottom panel); a phenotype described as "bunch boutons" [34]. This bunch bouton
123 phenotype in the trh^1/trh^2 mutant was detected at a high frequency; 18% of total
124 boutons were bunched compared to 3% for $trh^1/+$ and 0% for w^{1118} (Fig 1B). Of the
125 12 trh^1/trh^2 NMJs we examined, 11 possessed at least one bunch, with an average of 5
126 bunches per NMJ. Each bunch consisted of 3 to 10 small boutons (mean = 4.3). The
127 $trh^1/+$ larvae exhibited a much weaker phenotype; only 4 of 10 examined larvae had 1
128 or 2 bunches, with an average of 5 small boutons per bunch. We did not observe a
129 bunch bouton phenotype in any of the nine w^{1118} NMJs we assayed (Fig 1B).
130 Although the percentage of bunch boutons in the trh^1/trh^2 mutant was greatly
131 increased, total bouton number was only slightly higher than that observed in controls,
132 suggesting that bunch boutons form at the expense of normal ones (Fig 1B). We also
133 assessed the percentage of satellite boutons that are also small ones stemmed from
134 normal-size boutons, and are often observed in wild-type NMJs. We observed some
135 satellite boutons in the w^{1118} control and the trh^1/trh^2 mutant, and found no significant

differences between them (Fig S1A). Given the small size and clustering of synaptic boutons in the *trh*^{1}/*trh*^{2} mutant, we examined whether these bunch boutons express synaptic proteins normally. We found that the synaptic vesicle protein Synapsin (Syn in Fig 1A) was normally distributed relative to control, but the active zone protein Bruchpilot (Brp) was expressed at higher levels in bunch boutons (Fig S1B). The postsynaptic glutamate receptor, as revealed by GluRIIA (Fig S1C) and GluRIII (Fig S1B) signal, as well as dPAK (Fig S1C) were also localized in bunch boutons, which were surrounded by the subsynaptic reticulum protein Dlg (Fig S1D). Thus, although the Brp signal intensity in the *trh*^{1}/*trh*^{2} mutant was stronger than in the wild-type, the composition of synaptic proteins in bunch boutons was largely similar to that of normal-sized boutons.

As *trh* is expressed in both tracheal and nervous systems during embryonic stages [35], altered bouton morphology in the *trh*^{1}/*trh2* mutant could be due to a lack of *trh* in neurons, tracheal cells or other cells/tissues. Therefore, we performed *trh-RNAi* knockdown by using tissue-specific GAL4 drivers for trachea (*btl-GAL4*), neurons (*elav-GAL4*), glia (*repo-GAL4*), and muscles (*MHC-GAL4*). We observed a dramatic increase in bunch boutons upon tracheal *trh* knockdown using *btl-GAL4* (Fig 1C and 1D). In contrast, *trh-RNAi* alone or using *elav-GAL4*, *repo-GAL4* or *MHC-GAL4* failed to replicate the bunch bouton phenotype (Fig 1D).

To further confirm the necessity of tracheal *trh* for normal bouton formation, we performed a rescue experiment of the *trh*^{1}/*trh*^{2} phenotype. When we expressed a *UAS-trh* transgene in the trachea of the *trh*^{1}/*trh*^{2} mutant upon using the tracheal *btl-GAL4* driver, the bunch bouton phenotype was suppressed (Fig 1E and 1F). Controls bearing only the *btl-GAL4* driver or the *UAS-trh* transgene still contained the

160 comparably high numbers of bunch boutons observed in *trh*^{1}/*trh*^{2} (Fig 1B) or upon
161 tracheal *trh-RNAi* knockdown (Fig 1D). These results indicate that *trh* is required in
162 the trachea for normal bouton formation.

163

164 **Hypoxia induces bunch bouton formation**

165 Apart from specifying the tracheal cell fate, Trh is also involved in the
166 branching of tubular structures during post-embryonic stages [30]. Therefore, we
167 examined the tracheal phenotypes in the *trh*^{1}/*trh*^{2} larvae and observed an increase of
168 the number of terminal branches in the dorsal branch of the third segment (Fig S2A
169 and S2B). Furthermore, we identified morphological defects such as tracheal breaks
170 and tangles, suggesting structural defects in the *trh*^{1}/*trh*^{2} larvae (arrows in Fig S2A).
171 Tracheal branching activity is enhanced under hypoxia [18]. Thus, the increased
172 number of terminal branches in *trh*^{1}/*trh*^{2} could be a compensatory mechanism for
173 defective trachea formation.

174 To understand whether *trh*^{1}/*trh*^{2} mutant cells are under hypoxia, we used the
175 hypoxia biosensor GFP-ODD, in which the GFP is fused to the oxygen-dependent
176 degradation (ODD) domain of Sima, under the control of the *ubiquitin-69E* (*ubi*)
177 promoter [36]. We first confirmed that GFP-ODD signal was low under normoxia
178 (21% O_2) and enhanced under hypoxia (5% O_2, Fig 2A) in wild-type late-stage
179 embryos when tracheal tubules are already formed and functioning [36]. Indeed,
180 enhanced GFP signal was ubiquitous under hypoxia in wild-type embryos, with some
181 pronounced focal GFP signals (Fig 2A, upper row, and Fig S2C). The signal of
182 mRFP-nls, also under the control of *ubi* promoter as an internal control, remained
183 constant under hypoxia (Fig 2A, bottom row, and Fig S2D) [36]. Quantification of the

184 GFP/RFP ratio revealed a significant difference between normoxia and hypoxia
185 conditions (Fig 2B). We then examined whether oxygen supply is deficient in the
186 *trh*^{1}/*trh*^{2} mutant by measuring the GFP-ODD signals. We detected higher GFP-ODD
187 signal under hypoxia in the mutant compared to *w*^{1118} control (Fig 2A and Fig S2C).
188 The heterozygous *trh*^{1}/+ presented similar GFP-ODD signal to *w*^{1118}. Quantification
189 of the GFP/RFP ratio also demonstrated a significant increase in GFP-ODD signal in
190 *trh*^{1}/*trh*^{2} (Fig 2B), supporting that the *trh*^{1}/*trh*^{2} mutant senses reduced oxygen levels.

191 Thus, formation of bunch boutons in the *trh*^{1}/*trh*^{2} mutant could be caused by
192 hypoxia. To test this hypothesis, we reared wild-type larvae under hypoxia (5%) and
193 assessed synaptic bouton morphology at the third instar stage. Consistently, we
194 observed small clustered boutons, mirroring the bunch bouton phenotype, at NMJs
195 (Fig 2C and 2D). Furthermore, when we subjected the *trh*^{1}/*trh*^{2} mutant to a high
196 oxygen level (50%), the bunch bouton phenotype was completely suppressed, with
197 *trh*^{1}/*trh*^{2} NMJs exhibiting normal bouton morphology (Fig 2C and 2D). These results
198 suggest that hypoxia due to the defective tracheal system in the *trh*^{1}/*trh*^{2} mutant
199 induces the bunch bouton phenotype, and that this phenotype can be suppressed by
200 extra oxygen supply.

201

202 **Glial HIF-1α/Sima mediates bunch bouton formation**

203 HIF-1α/Sima mediates the response to low oxygen supply [37, 38]. Protein
204 levels of Sima are increased in wild-type *Drosophila* embryos subjected to hypoxia
205 [39], leading to transcriptional activation of downstream target genes and the
206 induction of tracheal branching [18]. We overexpressed Sima in tracheal cells,
207 neurons, glia, or muscle cells by tissue-specific drivers to investigate which types of
208 cells may play a role in modulating synaptic bouton formation. Overexpressing Sima

209 in trachea caused embryonic lethality, preventing us from observing NMJ phenotypes.
210 Larvae in which Sima was overexpressed in muscles, neurons, and glia could survive
211 to the third instar stage and we detected a substantial number of bunch boutons upon
212 glial Sima overexpression (Fig 3A and 3B). This result shows that the hypoxia-
213 responding factor Sima is capable of inducing bunch bouton formation when
214 overexpressed in glia.

215 If glial Sima is the factor responsible for responding to hypoxia in the *trh*^{1}/*trh*^{2}
216 mutant, reducing the Sima level in glia would suppress bunch bouton formation.
217 Accordingly, we expressed the *sima-RNAi* transgene, which could effectively deplete
218 *sima* expression (Fig S3A), using *repo-GAL4* in the *trh*^{1}/*trh*^{2} mutant. As our
219 prediction, the bunch bouton phenotype was almost completely suppressed upon glial
220 *sima* knockdown (Fig 3C and 3D). In controls, *trh*^{1}/*trh*^{2} mutants carrying only the
221 *UAS-sima-RNAi* transgene or the *repo-GAL4* driver still exhibited large numbers of
222 bunch boutons (Fig 3C and 3D). We also tested whether low oxygen level-induced
223 bunch bouton formation is mediated through Sima in glia. Bunch bouton phenotypes
224 were detected in controls carrying either *repo-GAL4* or *UAS-sima-RNAi* when raised
225 in 5% O_2 (Fig 3E). However, almost no bunch boutons were detected in larvae
226 carrying both *repo-GAL4* and *UAS-sima-RNAi* when raised in the same low-oxygen
227 environment (Fig 3E and 3F). We also examined Sima protein levels in larvae, and
228 found ubiquitous increases (including in Repo-positive glia) in the *trh*^{1}/*trh*^{2} mutant or
229 for the control under the 5% O_2 condition (Fig S3B). Thus, glial Sima mediates the
230 hypoxia response in the *trh*^{1}/*trh*^{2} mutant and in the low O_2 condition to modulate
231 synaptic bouton formation.

232

233 **Glial Wg remodels bouton morphology**

234 Next, we explored possible signals transduced from glia to neurons in
235 response to hypoxia. The glia-secreted Wingless (Wg) signaling molecule regulates
236 synaptic growth at *Drosophila* NMJs [40, 41]. Therefore, we examined whether Wg
237 can be induced under hypoxia in the trh^1/trh^2 mutant. Wg signal was enriched around
238 the synaptic boutons of wild-type NMJs (Fig 4A), similar to previous reported
239 staining patterns [40, 42]. Although the pattern of Wg signal at $trh^1/+$ NMJs was
240 similar to that of w^{1118}, we detected much higher levels of Wg at trh^1/trh^2 NMJs (Fig
241 4A). Quantification of Wg immunofluorescence intensities normalized to co-stained
242 HRP revealed a ~3-fold increase relative to w^{1118} and $trh^1/+$, respectively (Fig 4B).
243 We then examined whether Sima is required for the enhanced Wg expression in the
244 trh^1/trh^2 mutant. In a trh^1/trh^2 mutant carrying *repo-GAL4*, Wg levels were also
245 increased 3.0-fold relative to the *repo-GAL4* control (Fig 4C, 4D). When we reduced
246 *sima* levels in the trh^1/trh^2 mutant by *repo-GAL4*-driven *UAS-sima-RNAi*, Wg signal
247 was suppressed to a level equivalent to that in the *repo-GAL4* control (Fig 4C and 4D).
248 Interestingly, *sima-RNAi* knockdown in glia of the *repo-GAL4* control had no effect
249 on the Wg level (Fig 4C and 4D), suggesting that Sima is induced to upregulate Wg
250 expression in the trh^1/trh^2 mutant but has no role in basal Wg expression in the wild-
251 type. Taken together, we suggest that glial Sima is required for Wg upregulation at
252 the NMJs of the trh^1/trh^2 mutant.

253 If glia-secreted Wg is responsible for bunch bouton induction in the trh^1/trh^2
254 mutant, then glia-specific knockdown of *wg* in that mutant should suppress bunch
255 bouton formation. Indeed, the bunch bouton phenotype was almost undetectable in the
256 trh^1/trh^2 mutant also bearing *repo-GAL4* and the *UAS-wg-RNAi* transgene (Fig 4E and
257 4F). In control, bunch boutons were still prominent in the trh^1/trh^2 mutant bearing

258 only *UAS-wg-RNAi* (Fig 4E and 4F). Inactivation of Wg signaling has been shown to
259 induce unbundled filaments and a reduction of the more stabilized loops upon
260 immunostaining for the microtubule-binding protein Futsch [41, 43]. To show that
261 elevated Wg signaling remodels presynaptic bouton structure in the trh^1/trh^2 mutant,
262 we examined Futsch-labeled microtubules within synaptic boutons and found
263 significantly more Futsch-positive loops within the boutons (Fig S4A and S4B),
264 supporting the elevation of presynaptic Wg signaling. Taken together, these results
265 suggest that Wg plays a prominent role in the trh^1/trh^2 mutant to transduce the
266 hypoxia signal from glia to remodel presynaptic bouton structure.

267 Since glial processes can invade synaptic boutons to match the growth of
268 NMJs [44], we were intrigued to assess whether glia the trh^1/trh^2 mutant exhibits
269 morphological change. In a live preparation of NMJs, we found that glial processes
270 invaded the area of synaptic boutons in the trh^1/trh^2 mutant, whereas glial processes
271 were comparatively restrained in the control (Fig S4C). Quantification of fluorescent
272 signals of glial process overlaying the synaptic bouton area revealed significantly
273 greater area of overlap in the trh^1/trh^2 mutant relative to control (Fig S4D). This
274 increased extent of glial processes in the synaptic area may facilitate signal
275 transduction from glia to synaptic boutons for structural reorganization.

276

277 **Impaired crawling behavior in the *trh* mutant**

278 Given the evident morphological changes at trh^1/trh^2 NMJs, we wondered if
279 locomotion is affected in mutant larvae. We observed larvae crawling under free-
280 movement conditions and found that wild-type control and $trh^1/+$ heterozygous larvae
281 presented smooth crawling paths with an average speed of ~0.5 mm/s (Fig 5A and

282 5B), whereas the *trh*^{1}/*trh*^{2} larva had shorter paths and a slower speed of 0.14 mm/s.
283 The head turning frequency in *trh*^{1}/*trh*^{2} was comparable to both controls, not
284 contributing to the slow moving (Fig 5C). Larval crawling is a rhythmic behavior
285 involving a series of periodic strides (S1 Movie) [45-48]. We noticed uncoordinated
286 crawling in *trh*^{1}/*trh*^{2} larvae, with their posterior body segments failing to follow the
287 rhythmic movement (S2 Movie). We recorded larval forward crawling and
288 constructed kymographs to represent the stride cycle. In wild-type larvae, normal and
289 consistent periodic strides were apparent with regular head and tail displacements (Fig
290 5D, left panel). Similar to the wild-type, head movements of *trh*^{1}/*trh*^{2} larvae were
291 smooth and periodic, albeit slower. However, tail movements of *trh*^{1}/*trh*^{2} larvae were
292 abrupt (Fig 5D, right panel). Approximately 70% of the strides of *trh*^{1}/*trh*^{2} larvae
293 were uncoordinated (Fig 5E), which might contribute to the slower crawling of the
294 *trh*^{1}/*trh*^{2} mutant.

295 This uncoordinated stride cycle prompted us to examine the bouton
296 morphology in anterior and posterior segments of *trh*^{1}/*trh*^{2} larvae. Strikingly, we
297 detected the bunch bouton phenotype in segments A2-A4 of individual *trh*^{1}/*trh*^{2}
298 mutant larvae, whereas bouton morphology in their respective posterior A5 and A6
299 segments was relatively normal (Fig 6A). In fact, we seldom observed the bunch
300 bouton phenotype in posterior segments (Fig 6B). In wild-type larvae, all segments
301 we examined had normal bouton morphology (Fig 6A and 6B). While bunch boutons
302 appeared in A2-A4 segments, the total numbers of boutons were comparable in all
303 segments between wild-type and *trh*^{1}/*trh*^{2}. We further examined whether Wg signal
304 from glia has any effect on modifying bouton morphology in *trh*^{1}/*trh*^{2} larvae. Glial
305 *wg-RNAi* knockdown suppressed bunch bouton formation in the anterior A3 segment,

306 but had no effect on the morphological phenotype of the posterior A6 segment (Fig
307 6E). Thus, induction of bunch boutons is specific to anterior A2-A4 segments.

308 Given the bunch bouton phenotype in *trh*^{1}/*trh*^{2} larvae, we assessed basal
309 synaptic transmission properties, firstly at muscle 6 of anterior A3 segments.
310 Amplitude of evoked junctional potential (EJP), as well as the amplitude and
311 frequency of miniature EJP (mEJP), were comparable among controls and *trh*^{1}/*trh*^{2}
312 larvae (**Fig 7A-7E**). The quantal content, calculated by dividing the EJP amplitude
313 with that of mEJP, were also equivalent (**Fig 7F**). We then evaluated the synaptic
314 transmission properties of muscle 6 for posterior A6 segments. Although the
315 amplitude and frequency of mEJP and the EJP amplitude in *trh*^{1}/*trh*^{2} larvae remained
316 similar to controls, we did detect a significant reduction in the quantal content of
317 mutant larvae (**Fig 7F**). Thus, the impaired synaptic activity of posterior segments of
318 mutant larvae seems to be consistent with their defective stride cycle.

319 ## Discussion

320 Here, we demonstrate that Trh, a member of the NPAS protein family, non-cell
321 autonomously regulates synaptic bouton formation at NMJs through a hypoxia
322 response from glia. We observed small-sized and clustered boutons, so-called bunch
323 boutons, at the NMJs of *trh* mutant larvae or larvae reared at low oxygen levels. The
324 abnormal bouton morphology at *trh* NMJs could be suppressed by reducing levels of
325 the hypoxia response factor Sima in glia. We further showed that Sima enhanced the
326 Wg signal from glia to cause bunch bouton formation. Although normal synaptic
327 transmission was detected at NMJs located in anterior segments of larvae bearing
328 bunch boutons, reduced synaptic transmission was found in posterior segments
329 lacking bunch boutons of the *trh* mutant, suggesting that glia-induced bunch bouton
330 formation might be a homeostatic response to restore normal synaptic transmission.
331 Imbalanced synaptic functioning of mutant NMJs might contribute to the
332 uncoordinated stride cycles detected in the *trh* mutant, slowing larval crawl speed.
333 Thus, we provide a model for studying the glial responses that modulate synaptic
334 remodeling during hypoxia.

335

336 **Glia play a critical role in response to hypoxia in the *trh* mutant**

337 Animal cells adapt to hypoxia by triggering the expression of HIF-1α/Sima, the
338 master transcriptional regulator of the hypoxia response [49]. We observed defective
339 tracheal structure in the *trh* mutant (Fig S2A), which may result in hypoxic conditions
340 inside the larval body. The increase in terminal branch number (Fig S2B) may be a
341 response to oxygen supply deficiency [18]. Moreover, the increases in Sima protein
342 levels and *ODD-GFP* reporter expression indicate reduced internal oxygen levels (Fig

343 2A, 2B and S3B). Finally, the bunch bouton phenotype in the *trh* mutant was
344 recapitulated by rearing larvae under hypoxia, and it was suppressed by rearing larvae
345 under hyperoxia. Taken together, these observations suggest that cells in the *trh*
346 mutant sense low oxygen levels caused by the defective tracheal system and respond
347 by elevating Sima protein levels. It is not clear how profound this effect is for other
348 types of larval cells. Based on our ODD-GFP and Sima immunostaining patterns (Fig
349 2A, 2B and S3B), many types of cells are likely to be affected [50]. Our results also
350 suggest that Trh has a late developmental role in tracheal morphogenesis, in addition
351 to its well-characterized role in early tracheal cell fate specification [29, 30]. Unlike
352 the mammalian homologs NPAS1 and NPAS3 that function in the nervous system,
353 the *Drosophila* NPAS1/3 homolog Trh is more dedicated to tracheal development.

354

355 **Glia induce synaptic remodeling**

356 We suggest that glia is the major cell type mediating bunch bouton formation
357 in the *trh* mutant under hypoxia. HIF-1α/Sima was ubiquitously, including glia,
358 increased in both the trh^1/trh^2 mutant and the control grown under hypoxia (Fig S3B).
359 Importantly, by manipulating Sima expression in glia we could regulate bunch bouton
360 formation (Fig 3). Elevated Sima levels induce tracheal sprouting in tracheal cells, as
361 well as protrusions in non-tracheal cells [18]. Interestingly, we also observed
362 increased overlap of glial processes with synaptic area in the *trh* mutant, indicative of
363 a glial response (Fig S4C, S4D). Several types of cells in *Drosophila* have been
364 shown to respond to hypoxia [39, 51]. For instance, under hypoxia, elevated Sima
365 levels induce the expression of Breathless (Btl, the FGF receptor) in tracheal cells that
366 branch out seeking cells that express Branchless (Bnl)/FGF, with this latter process

367 also being partially dependent on Sima [18, 19]. In an alternative pathway, atypical
368 soluble guanylyl cyclases that are less sensitive to nitric oxide than conventional
369 soluble guanylyl cyclases can mediate graded and immediate hypoxia responses
370 mainly in neurons [52, 53]. *Drosophila* glia have not been reported to sense and
371 respond to hypoxia, but mammalian astrocytes in the central nervous system have
372 been shown to be involved in these processes. In a middle cerebral artery occlusion
373 mouse model, astrocyte activation was shown to play a crucial role in ischemic
374 tolerance, which is mediated through P2X7 receptor-activated HIF-1α upregulation
375 [24]. Under physiological hypoxia, reduced mitochondrial respiration leads to the
376 release of intracellular calcium and exocytosis of ATP-containing vesicles, thereby
377 signaling the brainstem to modulate animal breathing [54]. Our results reveal a role
378 for *Drosophila* larval glia in sensing hypoxia via the conventional HIF-1α/Sima
379 pathway, warranting further detailed study.

380 We also demonstrated that under hypoxia, glia modulate the formation of
381 synaptic boutons (Fig 3). These results clearly place the glia-modulated morphology
382 of synaptic boutons in the context of hypoxia responses. Several studies have
383 suggested that glia play important roles in regulating synaptic morphology at
384 developmental stages or in response to neural insult. Perisynaptic Schwann cells
385 surround nerve terminals and express neurotransmitter receptors, modulating synaptic
386 efficacy upon nerve stimulation at mouse NMJs [55]. After nerve injury, Schwann
387 cells participate in synaptic homeostasis and remodeling during NMJ re-innervation
388 [56]. Chronic hypoxia causes hypomyelination, leading to synaptic reduction in the
389 mouse cortex, which could be rescued by genetically-induced or drug-enhanced
390 hypermyelination [57]. In *Drosophila*, expansion of glial structures to synaptic
391 boutons matches synaptic growth [44]. Glial invasion of the synaptic region is also

392 suggested to clear presynaptic debris of unstable boutons during activity-dependent
393 synaptic growth [58]. Our study further establishes that in response to hypoxia, Wg is
394 a glial signal that modulates synaptic bouton formation. Two sources of Wg, from
395 presynaptic motor neurons and from glia, are involved in synapse growth and
396 remodeling [40]. Our results suggest that Sima upregulates the level of Wg secreted
397 from glia to modulate synapse formation in the *trh* mutant or in control larvae grown
398 under hypoxia. In hypoxic macrophages, HIF-1α mediates the induction of Wnt1,
399 which is a mammalian homolog of Wg [59-61]. Although it is unclear whether Wg is
400 a direct target of the hypoxia signal Sima in *Drosophila*, we show that the level of Wg
401 is controlled by glial Sima (Fig 4C, 4D) and that it mediates Sima-induced bunch
402 bouton formation at *trh* NMJs (Fig 4E, 4F). As a secreted morphogen, Wg functions
403 in both pre-synaptic and post-synaptic sites [41]. At presynaptic terminals, the
404 canonical Wg pathway induces microtubule loop formation to regulate synaptogenesis
405 [43]. We also detected an increase in microtubule loops in the *trh* mutant (Fig S4A,
406 S4B), consistent with a role for Wg in mediating the hypoxia response by modulating
407 synapse formation. Postsynaptic Wg signaling leads to subsynaptic reticulum
408 differentiation [41], which was not apparent in the *trh* mutant (Fig S1D), suggesting
409 that Wg might be a component of the complex hypoxia response that induces synapse
410 remodeling. Brief exposure to hypoxia induces immature spines and impaired
411 synaptic function in hippocampal neurons [23]. The morphological change to bunch
412 boutons at *trh* NMJs (Fig 1A and 1B) was not accompanied by altered synaptic
413 transmission (Fig 7A-F), which may reflect a compensatory effect during long-term
414 hypoxia.

415 The bunch bouton phenotype has also been described in *spastin* mutants [34, 62]. As
416 an AAA ATPase, Spastin severs microtubules to facilitate transport to distal axon

417 segments [63, 64]. Accordingly, the *spastin* mutant also exhibits a lack of
418 microtubules at terminal boutons [62]. In contrast, the *trh* mutant presented an
419 increase of microtubule loops (Fig S4A, S4B). Microtubule loops have been linked to
420 synaptic bouton stabilization, and an excess of microtubule loops has been associated
421 with increased synaptic bouton formation [65, 66]. The altered morphology of bunch
422 boutons may be part of the structural changes necessary to maintain normal synaptic
423 transmission under hypoxia. The *trh* and *spastin* mutants also exhibit differences in
424 synaptic function, with loss of *spastin* function slightly enhancing spontaneous
425 synaptic transmission release but reducing evoked synaptic transmission [62]. Thus,
426 although the morphology of synaptic boutons at *trh* NMJs resembles that of *spastin*
427 mutants, bunch boutons at *trh* NMJs retain synaptic functions, unlike the impaired
428 synaptic transmission of *spastin* mutant boutons.

429

430 **Difference of *trh* NMJs in anterior and posterior segments**

431 The size of NMJs in muscles 6/7 decreases from the anterior to posterior
432 segments, which could represent a coupling with muscle growth [67, 68], thereby
433 maintaining similar electrophysiological efficacy at anterior and posterior NMJs (Fig
434 7A-F). Interestingly, our findings show that synaptic responses in the *trh* mutant
435 differ, with bunch boutons only appearing in anterior segments (Fig 6A and 6B).
436 Furthermore, synaptic transmission at *trh* NMJs remained normal in anterior A3
437 segments but was impaired in posterior A6 segments (Fig 7A-F). These observations
438 are consistent with bunch bouton formation being part of a homeostatic response to
439 restore synaptic activity. Why synapses were not remodeled in posterior segments
440 remains unclear. Motor neurons in the ventral nerve cord project much longer axons

441 to muscles in posterior segments compared to anterior ones. It has been shown that
442 axonal transport to posterior segments is more vulnerable to inefficient transport
443 conditions. For example, mutation of long-chain Acyl-CoA synthetase impairs the
444 balance between anterograde and retrograde transport, causing distally-biased axonal
445 aggregations and affecting the growth and functioning of synapses [69]. In addition,
446 larval forward locomotion, propelled by peristatic contraction, is controlled by
447 different circuits targeting anterior and posterior segments. The GABAergic SEZ-
448 LN1 neurons specifically control posterior A6 and A7 segmental muscle contraction
449 by inhibiting A27h premotor neurons, which promotes longitudinal muscle
450 contraction during larval forward crawling [70]. It is possible that glia-derived Wg
451 signals from cell bodies located in the ventral nerve cord of the *trh* mutant may not be
452 efficiently transported to posterior segments during hypoxia. This polar difference in
453 synaptic activity and bouton morphology may contribute to the uncoordinated
454 peristatic movements of *trh* larvae.

455 # Methods

456 **Fly stocks**

457 All flies were reared at 25 °C. w^{1118} was used as wild-type control and to backcross
458 with trh^1 or trh^2. Fly strains are as follows: trh^2, *elav-GAL4*, *MHC-GAL4*, *repo-GAL4,*
459 *ok371-GAL4*, *UAS-trh*, *UAS-sima*, and *UAS-sima-RNAi* from Bloomington
460 Drosophila Stock Center (BDSC); trh^1 and *UAS-wg-RNAi* from Kyoto Stock Center,
461 and *UAS-trh-RNAi* from Vienna Drosophila Resource Center (VDRC). Also used
462 were *btl-GAL4* [71], *GFP-ODD* [36], and *the repo-cyto-GFP* line
463 was generated to drive cytoplasmic GFP expression under the control of the
464 4.3kb *repo* promoter, which recapitulates the full *repo* expression pattern. [72, 73]

465 **Hypoxia or hyperoxia rearing conditions**

466 Larvae in a food vial were transferred at 1 day after egg laying (AEL) to a ProOx
467 (model 110, BioSpherix, Lacona, NY) oxygen-controlled chamber. Oxygen or
468 nitrogen was infused into the chamber to a desired concentration (here, 5% or 50%),
469 which was maintained until assay.

470 **Immunostaining**

471 The NMJ phenotypes were analyzed as previously described [74]. For live tissue
472 preparation, non-fixed larvae were dissected as previously described, before directly
473 incubating larval fillets with anti-horseradish peroxidase (HRP, 1:10) in phosphate
474 buffered saline (PBS) for 10 minutes. Primary antibodies used were against Synapsin
475 (3C11, mouse, 1:100; Developmental Studies Hybridoma Bank, DSHB), HRP-Cy5
476 (rabbit, 1:100; Jackson ImmunoResearch), Dlg (mouse, 1:100, DSHB), GluRIIA
477 (mouse, 1:100, DSHB), dPAK (rabbit, 1:1000)[75], GluRIII (rabbit, 1:1000)[76], Brp
478 (nc82, mouse, 1:100, DHSB), Sima (guinea pig, 1:1000)[77], Repo (mouse, 1:1000,

479 DSHB), Wg (4D4, mouse, 1:10, DSHB), and Futsch (22C10, mouse, 1:100, DSHB).
480 Secondary antibodies used were anti-rabbit or -mouse 488, Cy3, or Cy5 (1:1000,
481 Jackson ImmunoResearch).

482 **Image acquisition and processing**

483 Unless specified otherwise, NMJs in muscle 6/7 of A3 segments of wandering third-
484 instar larvae were analyzed. Confocal images were acquired via LSM510 confocal
485 microscopy (Carl Zeiss) using 40x water, 40x water immersion, or 100x oil objectives.
486 All presented images are projections of confocal z-stacks. Numbers of bunch boutons,
487 total boutons, and microtubule loops were counted manually. The
488 immunofluorescence intensities of Wg and HRP, as well as the areas of GFP and HRP
489 signal, were analyzed in ImageJ. Each dot in the bar graph represents the data from a
490 single NMJ of a larva, and 8-10 NMJs from 2-5 independent experiments were pooled
491 for quantification. Embryos were acquired by means of LSM510 confocal microscopy
492 (Carl Zeiss) using a 20x objective, and were analyzed as previously described [36].
493 Each dot in the bar graph represents data from a single embryo in which fluorescence
494 was measured in at least 35 cells.

495 **Electrophysiological recordings**

496 Basal transmission properties were analyzed at NMJs of muscle 6/7 in specified
497 segments of wandering third-instar larvae as previously described [78], with some
498 modifications. The larval body wall was dissected in cold calcium-free HL3 solution
499 and recorded in HL3 solution containing 0.4 mM $CaCl_2$ at room temperature.

500 **Crawling behavior**

501 Mid third instar larvae (feeding stage) were placed on black agar plates (2% agar with
502 black food coloring in 25 × 20 cm^2 dishes) at room temperature for filming. Video

recording by a Sony Xperia Z1 camera started after 1 min habituation and lasted for 5 min, and it was analyzed using Ctrax software [79]. The (x, y) positions were used to calculate the crawling distance between two successive frames, and crawling speed was derived by dividing total distance travelled by time. The change in angle of larvae between two frames was divided by time to represent rotational speed. Our forward crawling assay was a modification of a previous study [48]. Larvae were transferred into a tunnel (~1 mm width) made in 2% black agar. Specimens were video-recorded for 3-10 mins using a Leica S8 APO microscope. Kymographs were constructed using the MultipleKymograph plug-in for ImageJ (NIH). Only forward crawling was counted, and 7-10 steps for each of ten larvae were analyzed for each genotype.

Acknowledgments

We thank S. Luschnig (Universität Münster), Y. Henry Sun (Academia Sinica), T Leung (National University of Singapore), A. DiAntonio (Washington University), BDSC, Kyoto Stock Center, VDRC, and DSHB for providing reagents; NPAS Electrophysiology Core, Taiwan Fly Core, and Hsiu-Hwa Kao for technical support; as well as Y.-J., Cheng, H. Li, V. Nithianandam and all members of C.-T. Chien's laboratory for discussion and comments.

Author contributions

Conceptualization: Pei-Yi Chen, Yi-Wei Tsai, Cheng-Ting Chien.

Formal analysis: Pei-Yi Chen.

Funding Acquisition: Cheng-Ting Chien

Investigation: Pei-Yi Chen.

Methodology: Pei-Yi Chen, Cheng-Ting Chien.

Project administration: Cheng-Ting Chien.

Resources: Pei-Yi Chen, Yi-Wei Tsai, Angela Giangrande, Cheng-Ting Chien.

Supervision: Cheng-Ting Chien.

Validation: Pei-Yi Chen.

Visualization: Pei-Yi Chen.

Writing – original draft: Pei-Yi Chen.

Writing – Review & Editing: Pei-Yi Chen, Yi-Wei Tsai, Angela Giangrande, Cheng-Ting Chien.

536 **References**

537 1. Larrivee B, Freitas C, Suchting S, Brunet I, Eichmann A. Guidance of
538 vascular development: lessons from the nervous system. Circ Res. 2009;104(4):428-
539 41. Epub 2009/02/28. doi: 10.1161/CIRCRESAHA.108.188144. PubMed PMID:
540 19246687.
541 2. Tam SJ, Watts RJ. Connecting vascular and nervous system development:
542 angiogenesis and the blood-brain barrier. Annu Rev Neurosci. 2010;33(1):379-408.
543 Epub 2010/04/07. doi: 10.1146/annurev-neuro-060909-152829. PubMed PMID:
544 20367445.
545 3. Banerjee S, Bhat MA. Neuron-glial interactions in blood-brain barrier
546 formation. Annu Rev Neurosci. 2007;30:235-58. Epub 2007/05/18. doi:
547 10.1146/annurev.neuro.30.051606.094345. PubMed PMID: 17506642; PubMed
548 Central PMCID: PMCPMC2824917.
549 4. Iadecola C. Neurovascular regulation in the normal brain and in Alzheimer's
550 disease. Nat Rev Neurosci. 2004;5(5):347-60. Epub 2004/04/22. doi:
551 10.1038/nrn1387. PubMed PMID: 15100718.
552 5. Zacchigna S, Lambrechts D, Carmeliet P. Neurovascular signalling defects in
553 neurodegeneration. Nat Rev Neurosci. 2008;9(3):169-81. Epub 2008/02/07. doi:
554 10.1038/nrn2336. PubMed PMID: 18253131.
555 6. Lee DL, Atkinson HJ. Physiology of nematodes: Macmillan International
556 Higher Education; 1976.
557 7. Manning G. Development of the Drosophila tracheal system. The
558 development of Drosophila melanogaster. 1993;1:609-85.
559 8. Danjo R, Kawasaki F, Ordway RW. A tripartite synapse model in Drosophila.
560 PLoS One. 2011;6(2):e17131. Epub 2011/03/02. doi: 10.1371/journal.pone.0017131.
561 PubMed PMID: 21359186; PubMed Central PMCID: PMCPMC3040228.
562 9. Semenza GL, Nejfelt MK, Chi SM, Antonarakis SE. Hypoxia-inducible
563 nuclear factors bind to an enhancer element located 3' to the human erythropoietin
564 gene. Proc Natl Acad Sci U S A. 1991;88(13):5680-4. Epub 1991/07/01. PubMed
565 PMID: 2062846; PubMed Central PMCID: PMCPMC51941.

566 10. Wang GL, Semenza GL. Purification and characterization of hypoxia-
567 inducible factor 1. J Biol Chem. 1995;270(3):1230-7. Epub 1995/01/20. PubMed
568 PMID: 7836384.
569 11. Stroka DM, Burkhardt T, Desbaillets I, Wenger RH, Neil DA, Bauer C, et al.
570 HIF-1 is expressed in normoxic tissue and displays an organ-specific regulation under
571 systemic hypoxia. FASEB J. 2001;15(13):2445-53. Epub 2001/11/02. doi:
572 10.1096/fj.01-0125com. PubMed PMID: 11689469.
573 12. Bruick RK, McKnight SL. A conserved family of prolyl-4-hydroxylases that
574 modify HIF. Science. 2001;294(5545):1337-40. Epub 2001/10/13. doi:
575 10.1126/science.1066373. PubMed PMID: 11598268.
576 13. Jaakkola P, Mole DR, Tian YM, Wilson MI, Gielbert J, Gaskell SJ, et al.
577 Targeting of HIF-alpha to the von Hippel-Lindau ubiquitylation complex by O2-
578 regulated prolyl hydroxylation. Science. 2001;292(5516):468-72. Epub 2001/04/09.
579 doi: 10.1126/science.1059796. PubMed PMID: 11292861.
580 14. Epstein AC, Gleadle JM, McNeill LA, Hewitson KS, O'Rourke J, Mole DR, et
581 al. C. elegans EGL-9 and mammalian homologs define a family of dioxygenases that
582 regulate HIF by prolyl hydroxylation. Cell. 2001;107(1):43-54. Epub 2001/10/12.
583 PubMed PMID: 11595184.
584 15. Groulx I, Lee S. Oxygen-dependent ubiquitination and degradation of
585 hypoxia-inducible factor requires nuclear-cytoplasmic trafficking of the von Hippel-
586 Lindau tumor suppressor protein. Mol Cell Biol. 2002;22(15):5319-36. Epub
587 2002/07/09. PubMed PMID: 12101228; PubMed Central PMCID: PMCPMC133938.
588 16. Huang LE, Arany Z, Livingston DM, Bunn HF. Activation of hypoxia-
589 inducible transcription factor depends primarily upon redox-sensitive stabilization of
590 its alpha subunit. J Biol Chem. 1996;271(50):32253-9. Epub 1996/12/13. PubMed
591 PMID: 8943284.
592 17. Kallio PJ, Pongratz I, Gradin K, McGuire J, Poellinger L. Activation of
593 hypoxia-inducible factor 1alpha: posttranscriptional regulation and conformational
594 change by recruitment of the Arnt transcription factor. Proc Natl Acad Sci U S A.
595 1997;94(11):5667-72. Epub 1997/05/27. PubMed PMID: 9159130; PubMed Central
596 PMCID: PMCPMC20836.
597 18. Centanin L, Dekanty A, Romero N, Irisarri M, Gorr TA, Wappner P. Cell
598 autonomy of HIF effects in Drosophila: tracheal cells sense hypoxia and induce
599 terminal branch sprouting. Dev Cell. 2008/04/16 ed2008. p. 547-58.

600 19. Jarecki J, Johnson E, Krasnow MA. Oxygen regulation of airway branching in
601 Drosophila is mediated by branchless FGF. Cell. 1999;99(2):211-20. Epub
602 1999/10/27. PubMed PMID: 10535739.
603 20. Ortega JA, Sirois CL, Memi F, Glidden N, Zecevic N. Oxygen Levels
604 Regulate the Development of Human Cortical Radial Glia Cells. Cereb Cortex.
605 2017;27(7):3736-51. Epub 2016/09/08. doi: 10.1093/cercor/bhw194. PubMed PMID:
606 27600849; PubMed Central PMCID: PMCPMC6075453.
607 21. O'Driscoll CM, Gorman AM. Hypoxia induces neurite outgrowth in PC12
608 cells that is mediated through adenosine A2A receptors. Neuroscience.
609 2005;131(2):321-9. Epub 2005/02/15. doi: 10.1016/j.neuroscience.2004.11.015.
610 PubMed PMID: 15708476.
611 22. Nikonenko I, Jourdain P, Muller D. Presynaptic remodeling contributes to
612 activity-dependent synaptogenesis. J Neurosci. 2003;23(24):8498-505. Epub
613 2003/09/19. PubMed PMID: 13679418.
614 23. Segura I, Lange C, Knevels E, Moskalyuk A, Pulizzi R, Eelen G, et al. The
615 Oxygen Sensor PHD2 Controls Dendritic Spines and Synapses via Modification of
616 Filamin A. Cell Rep. 2016;14(11):2653-67. Epub 2016/03/15. doi:
617 10.1016/j.celrep.2016.02.047. PubMed PMID: 26972007; PubMed Central PMCID:
618 PMCPMC4805856.
619 24. Hirayama Y, Ikeda-Matsuo Y, Notomi S, Enaida H, Kinouchi H, Koizumi S.
620 Astrocyte-mediated ischemic tolerance. J Neurosci. 2015;35(9):3794-805. Epub
621 2015/03/06. doi: 10.1523/JNEUROSCI.4218-14.2015. PubMed PMID: 25740510.
622 25. Stanco A, Pla R, Vogt D, Chen Y, Mandal S, Walker J, et al. NPAS1 represses
623 the generation of specific subtypes of cortical interneurons. Neuron. 2014;84(5):940-
624 53. Epub 2014/12/04. doi: 10.1016/j.neuron.2014.10.040. PubMed PMID: 25467980;
625 PubMed Central PMCID: PMCPMC4258152.
626 26. Pieper AA, Wu X, Han TW, Estill SJ, Dang Q, Wu LC, et al. The neuronal
627 PAS domain protein 3 transcription factor controls FGF-mediated adult hippocampal
628 neurogenesis in mice. Proc Natl Acad Sci U S A. 2005;102(39):14052-7. Epub
629 2005/09/21. doi: 10.1073/pnas.0506713102. PubMed PMID: 16172381; PubMed
630 Central PMCID: PMCPMC1216832.
631 27. Zhou S, Degan S, Potts EN, Foster WM, Sunday ME. NPAS3 is a trachealess
632 homolog critical for lung development and homeostasis. Proc Natl Acad Sci U S A.

633 2009;106(28):11691-6. Epub 2009/07/08. doi: 10.1073/pnas.0902426106. PubMed
634 PMID: 19581591; PubMed Central PMCID: PMCPMC2710647.
635 28. Levesque BM, Zhou S, Shan L, Johnston P, Kong Y, Degan S, et al. NPAS1
636 regulates branching morphogenesis in embryonic lung. Am J Respir Cell Mol Biol.
637 2007;36(4):427-34. Epub 2006/11/18. doi: 10.1165/rcmb.2006-0314OC. PubMed
638 PMID: 17110583; PubMed Central PMCID: PMCPMC1899329.
639 29. Chung S, Chavez C, Andrew DJ. Trachealess (Trh) regulates all tracheal
640 genes during Drosophila embryogenesis. Dev Biol. 2011;360(1):160-72. Epub
641 2011/10/04. doi: 10.1016/j.ydbio.2011.09.014. PubMed PMID: 21963537; PubMed
642 Central PMCID: PMCPMC3215829.
643 30. Wilk R, Weizman I, Shilo BZ. trachealess encodes a bHLH-PAS protein that
644 is an inducer of tracheal cell fates in Drosophila. Genes Dev. 1996;10(1):93-102.
645 Epub 1996/01/01. PubMed PMID: 8557198.
646 31. Jürgens G, Wieschaus E, Wieschaus Nüsslein-Volhard C, Kluding H.
647 Mutations affecting the pattern of the larval cuticle in Drosophila melanogaster. II.
648 Zygotic loci on the third chromosome1984. 283-95 p.
649 32. Chung S, Chavez C, Andrew DJ. Trachealess (Trh) regulates all tracheal
650 genes during Drosophila embryogenesis. Developmental Biology. 2011;360(1):160-
651 72. doi: https://doi.org/10.1016/j.ydbio.2011.09.014.
652 33. Younossi-Hartenstein A, Hartenstein V. The role of the tracheae and
653 musculature during pathfinding of Drosophila embryonic sensory axons.
654 Developmental Biology. 1993;158(2):430-47.
655 34. Ozdowski EF, Gayle S, Bao H, Zhang B, Sherwood NT. Loss of Drosophila
656 melanogaster p21-activated kinase 3 suppresses defects in synapse structure and
657 function caused by spastin mutations. Genetics. 2011;189(1):123-35. Epub
658 2011/06/28. doi: 10.1534/genetics.111.130831. PubMed PMID: 21705760; PubMed
659 Central PMCID: PMCPMC3176117.
660 35. Isaac DD, Andrew DJ. Tubulogenesis in Drosophila: a requirement for the
661 trachealess gene product. Genes Dev. 1996;10(1):103-17. Epub 1996/01/01. PubMed
662 PMID: 8557189.
663 36. Misra T, Baccino-Calace M, Meyenhofer F, Rodriguez-Crespo D, Akarsu H,
664 Armenta-Calderon R, et al. A genetically encoded biosensor for visualising hypoxia
665 responses in vivo. Biol Open. 2017;6(2):296-304. Epub 2016/12/25. doi:

666 10.1242/bio.018226. PubMed PMID: 28011628; PubMed Central PMCID:
667 PMCPMC5312090.
668 37. Centanin L, Gorr TA, Wappner P. Tracheal remodelling in response to
669 hypoxia. J Insect Physiol. 2010;56(5):447-54. Epub 2009/06/02. doi:
670 10.1016/j.jinsphys.2009.05.008. PubMed PMID: 19482033; PubMed Central PMCID:
671 PMCPMC2862287.
672 38. Wang GL, Jiang BH, Rue EA, Semenza GL. Hypoxia-inducible factor 1 is a
673 basic-helix-loop-helix-PAS heterodimer regulated by cellular O2 tension. Proc Natl
674 Acad Sci U S A. 1995;92(12):5510-4. Epub 1995/06/06. PubMed PMID: 7539918;
675 PubMed Central PMCID: PMCPMC41725.
676 39. Lavista-Llanos S, Centanin L, Irisarri M, Russo DM, Gleadle JM, Bocca SN,
677 et al. Control of the hypoxic response in Drosophila melanogaster by the basic helix-
678 loop-helix PAS protein similar. Mol Cell Biol. 2002;22(19):6842-53. Epub
679 2002/09/07. PubMed PMID: 12215541; PubMed Central PMCID: PMCPMC134029.
680 40. Kerr KS, Fuentes-Medel Y, Brewer C, Barria R, Ashley J, Abruzzi KC, et al.
681 Glial wingless/Wnt regulates glutamate receptor clustering and synaptic physiology at
682 the Drosophila neuromuscular junction. J Neurosci. 2014;34(8):2910-20. Epub
683 2014/02/21. doi: 10.1523/JNEUROSCI.3714-13.2014. PubMed PMID: 24553932;
684 PubMed Central PMCID: PMCPMC3931504.
685 41. Packard M, Koo ES, Gorczyca M, Sharpe J, Cumberledge S, Budnik V. The
686 Drosophila Wnt, wingless, provides an essential signal for pre- and postsynaptic
687 differentiation. Cell. 2002;111(3):319-30. Epub 2002/11/07. PubMed PMID:
688 12419243; PubMed Central PMCID: PMCPMC3499980.
689 42. Huang Y, Huang S, Di Scala C, Wang Q, Wandall HH, Fantini J, et al. The
690 glycosphingolipid MacCer promotes synaptic bouton formation in Drosophila by
691 interacting with Wnt. eLife. 2018;7:e38183. doi: 10.7554/eLife.38183.
692 43. Miech C, Pauer HU, He X, Schwarz TL. Presynaptic local signaling by a
693 canonical wingless pathway regulates development of the Drosophila neuromuscular
694 junction. J Neurosci. 2008;28(43):10875-84. Epub 2008/10/24. doi:
695 10.1523/JNEUROSCI.0164-08.2008. PubMed PMID: 18945895; PubMed Central
696 PMCID: PMCPMC2597682.
697 44. Brink DL, Gilbert M, Xie X, Petley-Ragan L, Auld VJ. Glial processes at the
698 Drosophila larval neuromuscular junction match synaptic growth. PLoS One.

699 2012;7(5):e37876. Epub 2012/06/06. doi: 10.1371/journal.pone.0037876. PubMed
700 PMID: 22666403; PubMed Central PMCID: PMCPMC3362601.
701 45. Hughes CL, Thomas JB. A sensory feedback circuit coordinates muscle
702 activity in Drosophila. Mol Cell Neurosci. 2007;35(2):383-96. Epub 2007/05/15. doi:
703 10.1016/j.mcn.2007.04.001. PubMed PMID: 17498969; PubMed Central PMCID:
704 PMCPMC1978164.
705 46. Lahiri S, Shen K, Klein M, Tang A, Kane E, Gershow M, et al. Two
706 alternating motor programs drive navigation in Drosophila larva. PLoS One.
707 2011;6(8):e23180. Epub 2011/08/23. doi: 10.1371/journal.pone.0023180. PubMed
708 PMID: 21858019; PubMed Central PMCID: PMCPMC3156121.
709 47. Dixit R, Vijayraghavan K, Bate M. Hox genes and the regulation of movement
710 in Drosophila. Dev Neurobiol. 2008;68(3):309-16. Epub 2007/11/30. doi:
711 10.1002/dneu.20589. PubMed PMID: 18044732.
712 48. Heckscher ES, Lockery SR, Doe CQ. Characterization of Drosophila larval
713 crawling at the level of organism, segment, and somatic body wall musculature. J
714 Neurosci. 2012;32(36):12460-71. Epub 2012/09/08. doi: 10.1523/JNEUROSCI.0222-
715 12.2012. PubMed PMID: 22956837; PubMed Central PMCID: PMCPMC3711835.
716 49. Semenza GL. Regulation of mammalian O_2 homeostasis by hypoxia-inducible
717 factor 1. Annu Rev Cell Dev Biol. 1999;15:551-78. Epub 1999/12/28. doi:
718 10.1146/annurev.cellbio.15.1.551. PubMed PMID: 10611972.
719 50. Ke Q, Costa M. Hypoxia-inducible factor-1 (HIF-1). Mol Pharmacol.
720 2006;70(5):1469-80. Epub 2006/08/05. doi: 10.1124/mol.106.027029. PubMed PMID:
721 16887934.
722 51. Arquier N, Vigne P, Duplan E, Hsu T, Therond PP, Frelin C, et al. Analysis of
723 the hypoxia-sensing pathway in Drosophila melanogaster. Biochem J. 2006;393(Pt
724 2):471-80. Epub 2005/09/24. doi: 10.1042/BJ20050675. PubMed PMID: 16176182;
725 PubMed Central PMCID: PMCPMC1360697.
726 52. Morton DB, Stewart JA, Langlais KK, Clemens-Grisham RA, Vermehren A.
727 Synaptic transmission in neurons that express the Drosophila atypical soluble
728 guanylyl cyclases, Gyc-89Da and Gyc-89Db, is necessary for the successful
729 completion of larval and adult ecdysis. J Exp Biol. 2008;211(Pt 10):1645-56. Epub
730 2008/05/06. doi: 10.1242/jeb.014472. PubMed PMID: 18456892; PubMed Central
731 PMCID: PMCPMC2424211.

732 53. Vermehren-Schmaedick A, Ainsley JA, Johnson WA, Davies SA, Morton DB.
733 Behavioral responses to hypoxia in Drosophila larvae are mediated by atypical
734 soluble guanylyl cyclases. Genetics. 2010;186(1):183-96. Epub 2010/07/02. doi:
735 10.1534/genetics.110.118166. PubMed PMID: 20592263; PubMed Central PMCID:
736 PMCPMC2940286.
737 54. Angelova PR, Kasymov V, Christie I, Sheikhbahaei S, Turovsky E, Marina N,
738 et al. Functional Oxygen Sensitivity of Astrocytes. J Neurosci. 2015;35(29):10460-73.
739 Epub 2015/07/24. doi: 10.1523/JNEUROSCI.0045-15.2015. PubMed PMID:
740 26203141; PubMed Central PMCID: PMCPMC4510287.
741 55. Colomar A, Robitaille R. Glial modulation of synaptic transmission at the
742 neuromuscular junction. Glia. 2004;47(3):284-9. Epub 2004/07/15. doi:
743 10.1002/glia.20086. PubMed PMID: 15252818.
744 56. Kang H, Tian L, Mikesh M, Lichtman JW, Thompson WJ. Terminal Schwann
745 cells participate in neuromuscular synapse remodeling during reinnervation following
746 nerve injury. J Neurosci. 2014;34(18):6323-33. Epub 2014/05/03. doi:
747 10.1523/JNEUROSCI.4673-13.2014. PubMed PMID: 24790203; PubMed Central
748 PMCID: PMCPMC4004816.
749 57. Wang F, Yang YJ, Yang N, Chen XJ, Huang NX, Zhang J, et al. Enhancing
750 Oligodendrocyte Myelination Rescues Synaptic Loss and Improves Functional
751 Recovery after Chronic Hypoxia. Neuron. 2018;99(4):689-701 e5. Epub 2018/08/07.
752 doi: 10.1016/j.neuron.2018.07.017. PubMed PMID: 30078577; PubMed Central
753 PMCID: PMCPMC6170028.
754 58. Fuentes-Medel Y, Logan MA, Ashley J, Ataman B, Budnik V, Freeman MR.
755 Glia and muscle sculpt neuromuscular arbors by engulfing destabilized synaptic
756 boutons and shed presynaptic debris. PLoS Biol. 2009;7(8):e1000184. Epub
757 2009/08/27. doi: 10.1371/journal.pbio.1000184. PubMed PMID: 19707574; PubMed
758 Central PMCID: PMCPMC2724735.
759 59. Mori H, Yao Y, Learman BS, Kurozumi K, Ishida J, Ramakrishnan SK, et al.
760 Induction of WNT11 by hypoxia and hypoxia-inducible factor-1alpha regulates cell
761 proliferation, migration and invasion. Sci Rep. 2016;6:21520. Epub 2016/02/11. doi:
762 10.1038/srep21520. PubMed PMID: 26861754; PubMed Central PMCID:
763 PMCPMC4748282.
764 60. Swarup S, Verheyen EM. Wnt/Wingless signaling in Drosophila. Cold Spring
765 Harb Perspect Biol. 2012;4(6):a007930. Epub 2012/04/27. doi:

766 10.1101/cshperspect.a007930. PubMed PMID: 22535229; PubMed Central PMCID:
767 PMCPMC3367557.
768 61. Ortiz-Masia D, Cosin-Roger J, Calatayud S, Hernandez C, Alos R, Hinojosa J,
769 et al. Hypoxic macrophages impair autophagy in epithelial cells through Wnt1:
770 relevance in IBD. Mucosal Immunol. 2014;7(4):929-38. Epub 2013/12/05. doi:
771 10.1038/mi.2013.108. PubMed PMID: 24301659.
772 62. Sherwood NT, Sun Q, Xue M, Zhang B, Zinn K. Drosophila spastin regulates
773 synaptic microtubule networks and is required for normal motor function. PLoS Biol.
774 2004;2(12):e429. Epub 2004/11/25. doi: 10.1371/journal.pbio.0020429. PubMed
775 PMID: 15562320; PubMed Central PMCID: PMCPMC532392.
776 63. Hazan J, Fonknechten N, Mavel D, Paternotte C, Samson D, Artiguenave F, et
777 al. Spastin, a new AAA protein, is altered in the most frequent form of autosomal
778 dominant spastic paraplegia. Nat Genet. 1999;23(3):296-303. Epub 1999/12/28. doi:
779 10.1038/15472. PubMed PMID: 10610178.
780 64. Karabay A, Yu W, Solowska JM, Baird DH, Baas PW. Axonal growth is
781 sensitive to the levels of katanin, a protein that severs microtubules. J Neurosci.
782 2004;24(25):5778-88. Epub 2004/06/25. doi: 10.1523/JNEUROSCI.1382-04.2004.
783 PubMed PMID: 15215300.
784 65. Roos J, Hummel T, Ng N, Klambt C, Davis GW. Drosophila Futsch regulates
785 synaptic microtubule organization and is necessary for synaptic growth. Neuron.
786 2000;26(2):371-82. Epub 2000/06/06. PubMed PMID: 10839356.
787 66. Franco B, Bogdanik L, Bobinnec Y, Debec A, Bockaert J, Parmentier ML, et
788 al. Shaggy, the homolog of glycogen synthase kinase 3, controls neuromuscular
789 junction growth in Drosophila. J Neurosci. 2004;24(29):6573-7. Epub 2004/07/23. doi:
790 10.1523/JNEUROSCI.1580-04.2004. PubMed PMID: 15269269.
791 67. Koch I, Schwarz H, Beuchle D, Goellner B, Langegger M, Aberle H.
792 Drosophila ankyrin 2 is required for synaptic stability. Neuron. 2008;58(2):210-22.
793 Epub 2008/04/29. doi: 10.1016/j.neuron.2008.03.019. PubMed PMID: 18439406.
794 68. Nijhof B, Castells-Nobau A, Wolf L, Scheffer-de Gooyert JM, Monedero I,
795 Torroja L, et al. A New Fiji-Based Algorithm That Systematically Quantifies Nine
796 Synaptic Parameters Provides Insights into Drosophila NMJ Morphometry. PLoS
797 Comput Biol. 2016;12(3):e1004823. Epub 2016/03/22. doi:
798 10.1371/journal.pcbi.1004823. PubMed PMID: 26998933; PubMed Central PMCID:
799 PMCPMC4801422.

800 69. Liu Z, Huang Y, Zhang Y, Chen D, Zhang YQ. Drosophila Acyl-CoA
801 synthetase long-chain family member 4 regulates axonal transport of synaptic vesicles
802 and is required for synaptic development and transmission. J Neurosci.
803 2011;31(6):2052-63. Epub 2011/02/11. doi: 10.1523/JNEUROSCI.3278-10.2011.
804 PubMed PMID: 21307243.
805 70. Tastekin I, Khandelwal A, Tadres D, Fessner ND, Truman JW, Zlatic M, et al.
806 Sensorimotor pathway controlling stopping behavior during chemotaxis in the
807 Drosophila melanogaster larva. Elife. 2018;7. Epub 2018/11/23. doi:
808 10.7554/eLife.38740. PubMed PMID: 30465650; PubMed Central PMCID:
809 PMCPMC6264072.
810 71. Shiga Y, Tanaka-Matakatsu M, Hayashi S. A nuclear GFP/β-galactosidase
811 fusion protein as a marker for morphogenesis in living Drosophila. Dev Growth
812 Differ. 1996;38(1):99-106.
813 72. Lee BP, Jones BW. Transcriptional regulation of the Drosophila glial gene
814 repo. Mech Dev. 2005;122(6):849-62. Epub 2005/06/09. doi:
815 10.1016/j.mod.2005.01.002. PubMed PMID: 15939231.
816 73. Laneve P, Delaporte C, Trebuchet G, Komonyi O, Flici H, Popkova A, et al.
817 The Gcm/Glide molecular and cellular pathway: new actors and new lineages. Dev
818 Biol. 2013;375(1):65-78. Epub 2013/01/02. doi: 10.1016/j.ydbio.2012.12.014.
819 PubMed PMID: 23276603.
820 74. Wang M, Chen PY, Wang CH, Lai TT, Tsai PI, Cheng YJ, et al. Dbo/Henji
821 Modulates Synaptic dPAK to Gate Glutamate Receptor Abundance and Postsynaptic
822 Response. PLoS Genet. 2016;12(10):e1006362. Epub 2016/10/14. doi:
823 10.1371/journal.pgen.1006362. PubMed PMID: 27736876; PubMed Central PMCID:
824 PMCPMC5065118.
825 75. Harden N, Lee J, Loh HY, Ong YM, Tan I, Leung T, et al. A Drosophila
826 homolog of the Rac- and Cdc42-activated serine/threonine kinase PAK is a potential
827 focal adhesion and focal complex protein that colocalizes with dynamic actin
828 structures. Mol Cell Biol. 1996;16(5):1896-908. Epub 1996/05/01. PubMed PMID:
829 8628256; PubMed Central PMCID: PMCPMC231177.
830 76. Marrus SB, Portman SL, Allen MJ, Moffat KG, DiAntonio A. Differential
831 localization of glutamate receptor subunits at the Drosophila neuromuscular junction.

832 J Neurosci. 2004;24(6):1406-15. Epub 2004/02/13. doi: 10.1523/JNEUROSCI.1575-
833 03.2004. PubMed PMID: 14960613.
834 77. Wang CW, Purkayastha A, Jones KT, Thaker SK, Banerjee U. In vivo genetic
835 dissection of tumor growth and the Warburg effect. Elife. 2016;5:e18126. Epub
836 2016/09/02. doi: 10.7554/eLife.18126. PubMed PMID: 27585295; PubMed Central
837 PMCID: PMCPMC5030086.
838 78. Tsai PI, Kao HH, Grabbe C, Lee YT, Ghose A, Lai TT, et al. Fak56 functions
839 downstream of integrin alphaPS3betanu and suppresses MAPK activation in
840 neuromuscular junction growth. Neural Dev. 2008;3:26. Epub 2008/10/18. doi:
841 10.1186/1749-8104-3-26. PubMed PMID: 18925939; PubMed Central PMCID:
842 PMCPMC2576229.
843 79. Branson K, Robie AA, Bender J, Perona P, Dickinson MH. High-throughput
844 ethomics in large groups of Drosophila. Nat Methods. 2009;6(6):451-7. Epub
845 2009/05/05. doi: 10.1038/nmeth.1328. PubMed PMID: 19412169; PubMed Central
846 PMCID: PMCPMC2734963.
847

848 **Figure legends**

849 **Fig 1. Bunch bouton formation at *trh* NMJs**

850 (A, C, E) Immunostaining images show NMJs of muscle 6/7 for Syn (green) and HRP
851 (red) in w^{1118}, $trh^1/+$, and trh^1/trh^2 (A), *btl-GAL4* and *btl-GAL4/trh-RNAi* (C), and
852 *UAS-trh* trh^1/trh^2, *btl-GAL4* trh^1/trh^2, *btl-GAL4/UAS-trh* trh^1/trh^2 (E). Dashed squares
853 in (A) are enlarged in right panels. White arrows indicate clusters of bunch boutons.
854 Scale bars are 10 μm. (B, D, F) Bar graphs with data dots within each bar show
855 percentages (mean ± standard error of mean, SEM) of bunch boutons to total boutons.
856 (B) w^{1118}, 0 ± 0%, n = 10; $trh^1/+$, 3.64 ± 1.74%, n = 10; trh^1/trh^2, 18.04 ± 3.65%, n =
857 10. (D) *trh-RNAi* , 0 ± 0%, n = 10; *btl-GAL4*, 0 ± 0%, n = 10; *btl>trh-RNAi*, 8.64 ±
858 2.81%, n = 9; *elav-GAL4*, 0 ± 0%, n = 10; *elav>trh-RNAi*, 0 ± 0%, n = 10; *repo-GAL4*,
859 2.14 ± 1.56%, n = 10; *repo>trh-RNAi*, 0 ± 0%, n = 10; *MHC-GAL4*, 0 ± 0%, n = 10;
860 *MHC>trh-RNAi*, 0.77 ± 0.77%, n = 10. (F) *UAS-trh* trh^1/trh^2, 13.80 ± 3.00%, n = 10;
861 *btl-GAL4* trh^1/trh^2, 13.56 ± 2.95%, n = 10; *btl-GAL4/UAS-trh* trh^1/trh^2, 0.88 ± 0.64%,
862 n = 8. (B, bottom panel) Total bouton numbers in w^{1118} (74.10 ± 4.72, n = 10), $trh^1/+$
863 (89.60 ± 5.16, n = 10), and trh^1/trh^2 (95.00 ± 11.21, n = 9). Statistical significance by
864 Mann-Whitney test is shown as n.s., no significance; *, $p < 0.5$; **, $p < 0.01$; ***, $p <$
865 0.001.

866

867 **Fig 2. Induction of bunch boutons in *trh* mutants by hypoxia**

868 (A) Images of late-stage embryos of w^{1118}, $trh^1/+$, and trh^1/trh^2 carrying the *GFP-*
869 *ODD* reporter (top row) and *mRFP-nls* control (bottom row) under normoxia (21% O_2)
870 or hypoxia (5% O_2). Scale bar represents 40 μm. (B) Bar graphs show mean ± SEM of
871 the GFP/RFP immunofluorescence intensity ratio (w^{1118} at 21% O_2, 0.18 ± 0.05, n = 6;

872 w^{1118} at 5% O_2, 0.84 ± 0.15, n = 6; trh^1/+ at 21% O_2, 0.09 ± 0.02, n = 6; trh^1/trh^2 at
873 21% O_2, 0.82 ± 0.15, n = 6). Statistical significance by Mann-Whitney test is shown
874 as n.s., no significance; **, $p < 0.01$; ***, $p < 0.001$. (C) Images of NMJs from
875 muscle 6/7 immunostained for Syn (green) and HRP (red) from w^{1118} at 21% or 5%
876 O_2 (left panels) and trh^1/trh^2 (right panels) at 21% or 50% O_2. White arrows indicate
877 clusters of bunch boutons. Scale bar represents 10 μm. (D) Bar graph shows
878 percentages (mean ± SEM) of bunch boutons to total boutons (w^{1118} at 21% O_2, 0 ±
879 0%, n = 10; w^{1118} at 5% O_2, 8.47 ± 1.78%, n = 10; trh^1/trh^2 at 21% O_2, 12.91 ± 2.30%,
880 n = 10; trh^1/trh^2 at 50% O_2, 0 ± 0%, n = 10). Statistical significance by Mann-
881 Whitney test is shown as ***, $p < 0.001$.

882

883 **Fig 3. Bunch bouton induction by glial Sima at *trh* NMJs**

884 (A, C, E) Images showing NMJs from muscle 6/7 immunostained for Syn (green) and
885 HRP (red) in *repo-GAL4,* and *repo-GAL4/UAS-sima* (A), *sima-RNAi* trh^1/trh^2, *repo-*
886 *GAL4* trh^1/trh^2, and *repo-GAL4/sima-RNAi* trh^1/trh^2 (C), *sima-RNAi*, *repo-GAL4*, and
887 *repo-GAL4*/*sima-RNAi* under hypoxia at 5% O_2 (E). White arrows indicate bunch
888 boutons. Scale bars represent 10 μm. (B, D, F) Bar graphs show percentages (mean ±
889 SEM) of bunch boutons (B) *ok371-GAL4*/*UAS-sima*, 0.31 ± 0.31%, n = 10; *repo-*
890 *GAL4*/*UAS-sima*, 8.81 ± 2.22%, n = 10; *MHC-GAL4*/*UAS-sima*, 1.19 ± 0.64%, n = 10.
891 (D) *sima-RNAi* trh^1/trh^2, 7.48 ± 1.35%, n = 10; *repo-GAL4* trh^1/trh^2, 11.56 ± 2.17%, n
892 = 10; *repo-GAL4/sima-RNAi* trh^1/trh^2, 1.58 ± 0.81%, n = 10. (F) *sima-RNAi* at 5% O_2,
893 11.14 ± 2.8%, n = 11; *repo-GAL4* at 5% O_2, 12.65 ± 2.66%, n = 10; *repo-GAL4*/*sima-*
894 *RNAi* at 5% O_2, 0.45 ± 0.45%, n = 11. Statistical significance by one-way ANOVA
895 with Tukey's Multiple Comparison post test is shown as ***, $p < 0.001$ (B) or Mann-
896 Whitney test as n.s., no significance; **, $p < 0.01$; ***, $p < 0.001$ (D, F).

897

898 **Fig 4. Wg induction from glia modulates synaptogenesis at *trh* NMJs**

899 (A, C, E) Images showing NMJs of muscle 6/7 immunostained for Wg (green) and
900 HRP (red) in w^{1118}, $trh^1/+$, and trh^1/trh^2 (A); *repo-GAL4*, *repo-GAL4/sima-RNAi,*
901 *repo-GAL4* trh^1/trh^2, and *repo-GAL4/sima-RNAi* trh^1/trh^2 (C); and for Syn (green)
902 and HRP (red) in *wg-RNAi* trh^1/trh^2 and *repo-GAL4/wg-RNAi* trh^1/trh^2 (E). White
903 arrows indicate clusters of bunch boutons. Scale bars represent 10 μm. (B, D, F) Bar
904 graphs show averages (mean ± SEM) of normalized Wg to HRP intensities. w^{1118},
905 0.18 ± 0.03, n = 8; $trh^1/+$, 0.15 ± 0.02, n = 9; trh^1/trh^2, 0.49 ± 0.07, n = 9 (B), *repo-*
906 *GAL4*, 0.23 ± 0.04, n = 11; *repo-GAL4/sima-RNAi*, 0.25 ± 0.02, n = 10; *repo-GAL4*
907 trh^1/trh^2, 0.68 ± 0.16, n = 8; *repo-GAL4/sima-RNAi* trh^1/trh^2, 0.25 ± 0.05, n = 9 (D),
908 and percentages (mean ± SEM) of bunch boutons in *wg-RNAi* trh^1/trh^2, 17.19 ±
909 3.52%, n = 8; *repo-GAL4/wg-RNAi* trh^1/trh^2, 0.68 ± 0.68%, n = 11 (F). Statistical
910 significance by Mann-Whitney test is shown as n.s., no significance; *, $p < 0.05$; **, p
911 < 0.01; ***, $p < 0.001$.

912

913 **Fig 5. Impaired crawling behavior of the *trh* mutant**

914 (A) Representative 5-minute crawling traces for w^{1118}, $trh^1/+$, and trh^1/trh^2. (B) Bar
915 graphs show average speeds (mean ± SEM in mm/s) for w^{1118}, 0.64 ± 0.09, n = 13;
916 $trh^1/+$, 0.45 ± 0.08, n = 12; trh^1/ trh^2, 0.14 ± 0.02, n = 14, and average rotational
917 speeds (mean ± SEM in degree/s) for w^{1118}, 7.80 ± 0.62, n = 13; $trh^1/+$, 9.73 ± 1.19, n
918 = 12; trh^1/trh^2, 11.26 ± 1.86, n = 14. Statistical significance by Mann-Whitney test is
919 shown as n.s., no significance; ***, $p < 0.001$. (D) Kymographs show four larval
920 forward crawling strides for w^{1118} and trh^1/trh^2. The green lines show smooth
921 transitions between successive strides, whereas orange lines show abrupt transitions.

922 (E) Bar graph shows uncoordinated stride percentages (mean ± SEM) in w^{1118} (0 ±
923 0%, n = 10) and trh^1/trh^2 (69.22 ± 9.57%, n = 10). Statistical significance by Mann-
924 Whitney test is shown as ***, $p < 0.001$.

925

926 **Fig 6. Selective bunch bouton formation at *trh* NMJs of anterior segments**

927 (A) Images show NMJs of muscle 6/7 from abdominal segments A2-A6
928 immunostained for Syn (green) and HRP (red) in w^{1118} and trh^1/ trh^2. White arrows
929 indicate clusters of bunch boutons. Scale bar represents 10 μm. (B, C) Line graphs
930 show average percentages (mean ± SEM) of (B) bunch bouton (w^{1118}: A2, 0 ± 0%, n =
931 10; A3, 0 ± 0%, n = 9; A4, 0 ± 0%, n = 10; A5, 0 ± 0%, n = 10; A6, 0 ± 0%, n = 9;
932 trh^1/trh^2: A2, 15.40 ± 3.59%, n = 10; A3, 19.80 ± 3.09%, n = 10; A4, 5.11 ± 1.86%, n
933 = 9; A5, 0.80 ± 0.80%, n = 10; A6, 1.33 ± 1.33%, n = 9) and total bouton numbers
934 (w^{1118}: A2, 176.60 ± 15.00, n = 10; A3, 76.11 ± 4.77, n = 9; A4, 85.80 ± 4.13, n = 10;
935 A5, 66.10 ± 5.39, n = 10; A6, 40.00 ± 3.72, n = 9; trh^1/trh^2: A2, 173.20 ± 8.76, n = 10;
936 A3, 106.60 ± 15.33, n = 10; A4, 74.11 ± 9.90, n = 9; A5, 60.70 ± 9.10, n = 10; A6,
937 33.11 ± 3.56, n = 9) for w^{1118} (magenta lines) and trh^1/ trh^2 (blue lines). Statistical
938 significance by Mann-Whitney test is shown as n.s., no significance; *, $p < 0.05$; ***,
939 $p < 0.001$. (D) Images showing NMJs of muscle 6/7 immunostained for Syn (green)
940 and HRP (red) in *wg-RNAi* trh^1/trh^2 (top panel) and *repo-GAL4/wg-RNAi* trh^1/trh^2
941 (bottom panel) in A6. (D) Bar graph shows percentages (mean ± SEM) of bunch
942 boutons (*wg-RNAi* trh^1/trh^2, 1.60 ± 1.60%, n = 10; *repo-GAL4/wg-RNAi* trh^1/trh^2, 0 ±
943 0%, n = 10). Statistical significance by Mann-Whitney test is shown as n.s., no
944 significance.

945

946 **Fig 7. Synaptic transmission at *trh* NMJs.**

947 (A, B) Representative traces of mEJPs (A) and EJPs (B) recorded from NMJs of
948 muscle 6 of segment A3 (left panels) and A6 (right panels) for w^{1118} and trh^1/trh^2. The
949 scales for both mEJP and EJP traces are depicted at right. (C-F) Bar graphs show
950 averages (mean ± SEM) for (C) mEJP amplitudes (w^{1118}/A3, 1.43 ± 0.11, n = 10;
951 trh^1/trh^2/A3, 1.19 ± 0.12, n = 13; w^{1118}/A6, 1.25 ± 0.11, n = 9; trh^1/trh^2/A6, 1.51 ±
952 0.20, n = 8); (D) mEJP frequencies (w^{1118}/A3, 1.92 ± 0.13, n = 10; trh^1/trh^2/A3, 2.38 ±
953 0.27, n = 13; w^{1118}/A6, 2.02 ± 0.34, n = 9; trh^1/trh^2/A6, 1.41 ± 0.21, n = 8); (E) EJP
954 amplitudes (w^{1118}/A3, 54.61 ± 2.06, n = 10; trh^1/trh^2/A3, 50.89 ± 4.18, n = 13;
955 w^{1118}/A6, 46.24 ± 3.71, n = 9; trh^1/trh^2/A6, 41.64 ± 5.71, n = 8); and (F) quantal
956 contents (QC) calculated as EJP/mEJP (w^{1118}/A3, 40.23 ± 3.33, n = 10; trh^1/trh^2/A3,
957 49.63 ± 3.91, n = 13; w^{1118}/A6, 38.90 ± 3.75, n = 9; trh^1/trh^2/A6, 27.88 ± 1.53, n = 8).
958 Statistical significance by Mann-Whitney test is shown as n.s., no significance; *, $p < 0.05$;
959 **, $p < 0.01$.
960

961 ## Supporting information

962 **S1 Fig. Presynaptic and postsynaptic structures in *trh* mutants**

963 (A) Bar graphs show percentages (mean ± SEM) of satellite boutons to total boutons
964 (w^{1118}, 5.13 ± 1.66%, n = 10; trh^1/+, 0.66 ± 0.66%, n = 10; trh^1/trh^2, 2.63 ± 0.97%, n
965 = 10). Statistical significance by Mann-Whitney test is shown as n.s., no significance;
966 *, $p < 0.5$. (B, C, D) Images showing NMJs of muscle 6/7 immunostained for Brp,
967 GluRIII, and HRP (B), GluRIIA, dPAK, and HRP (C), and Dlg and HRP (D) in w^{1118},
968 trh^1/+, and trh^1/trh^2. Scale bars are 10 μm.

969

970 **S2 Fig. Tracheal defects in *trh* mutants**

971 (A) A bright-field view of tracheal dorsal branches of trh^1/+ (left top panel) and
972 trh^1/trh^2 (right top panel), and tracheal dorsal trunks of trh^1/trh^2 (bottom panels).
973 Numbers denote terminal branches, and arrows indicate a tracheal break (bottom left)
974 and a tracheal tangle (bottom right). Scale bar represents 50 μm. (B) Bar graph shows
975 mean ± SEM of dorsal terminal branches (trh^1/+, 5.70 ± 0.15, n = 10; trh^1/trh^2, 7.55 ±
976 0.28, n = 11). (C) Bar graphs show mean ± SEM of the GFP immunofluorescence
977 intensity (w^{1118} at 21% O_2, 20.33 ± 7.54, n = 6; w^{1118} at 5% O_2, 79.31 ± 17.98, n = 6;
978 trh^1/+ at 21% O_2, 13.29 ± 3.64, n = 6; trh^1/trh^2 at 21% O_2, 108.2 ± 14.70, n = 6). (D)
979 Bar graphs show mean ± SEM of RFP immunofluorescence intensity (w^{1118} at 21% O_2,
980 102.00 ± 15.55, n = 6; w^{1118} at 5% O_2, 109.60 ± 13.12, n = 6; trh^1/+ at 21% O_2,
981 143.00 ± 15.67, n = 6; trh^1/trh^2 at 21% O_2, 151.50 ± 16.77, n = 6). Statistical
982 significance by Mann-Whitney test is shown as n.s., no significance; **, $p < 0.01$; ***,
983 $p < 0.001$.

984

985 **S3 Fig. Efficiency of *sima-RNAi* knockdown and Sima upregulation**

986 (A) Assay for *sima* mRNA levels in *da-GAL4* (control) or *da-GAL4/sima-RNAi* shows
987 a reduction upon *sima-RNAi* knockdown. The *Rpl19* mRNA levels are comparable in
988 both genotypes. (B) Images showing central nerve cord immunostained for Sima
989 (green) and Repo (red) in w^{1118} at 21% O_2, w^{1118} at 5% O_2, and trh^1/trh^2 at 21% O_2.
990 Arrows indicate glia with high Sima protein levels. Scale bar represents 20 µm.

991

992 **S4 Fig. Microtubule loops and glial invasion of *trh* NMJs**

993 (A) Images showing NMJs of muscle 6/7 immunostained for HRP (red) and Futsch
994 (green) in trh^1/+ and trh^1/ trh^2. White arrows indicate microtubule loops. Dashed
995 squares are enlarged in right panels. Scale bar represents 10 µm. (B) Bar graphs show
996 averages (mean ± SEM) of Futsch loops (trh^1/+, 2.92 ± 0.29, n = 12; trh^1/ trh^2, 9.56 ±
997 1.11, n = 9). (C) 3D images of live tissues showing NMJs of muscle 6/7 carrying
998 *repo-cyto-GFP* (green) labeled for HRP (red) in trh^1/+ and trh^1/trh^2 by using Imaris.
999 Synaptic overlap by glia is represented in yellow. Scale bar represents 10 µm. (D) Bar
1000 graph shows percentages (mean ± SEM) of synaptic areas overlapping with glia in
1001 trh^1/+, 6.2 ± 0.99%, n = 10; trh^1/trh^2, 16.7 ± 3.66, n = 10. Statistical significance by
1002 Mann-Whitney test is shown as *, $p < 0.05$ or ***, $p < 0.001$.

1003

1004 **S1 Movie. Forward crawling of w^{1118}**

1005

1006 **S2 Movie. Forward crawling of trh^1/trh^2**

Fig. 1

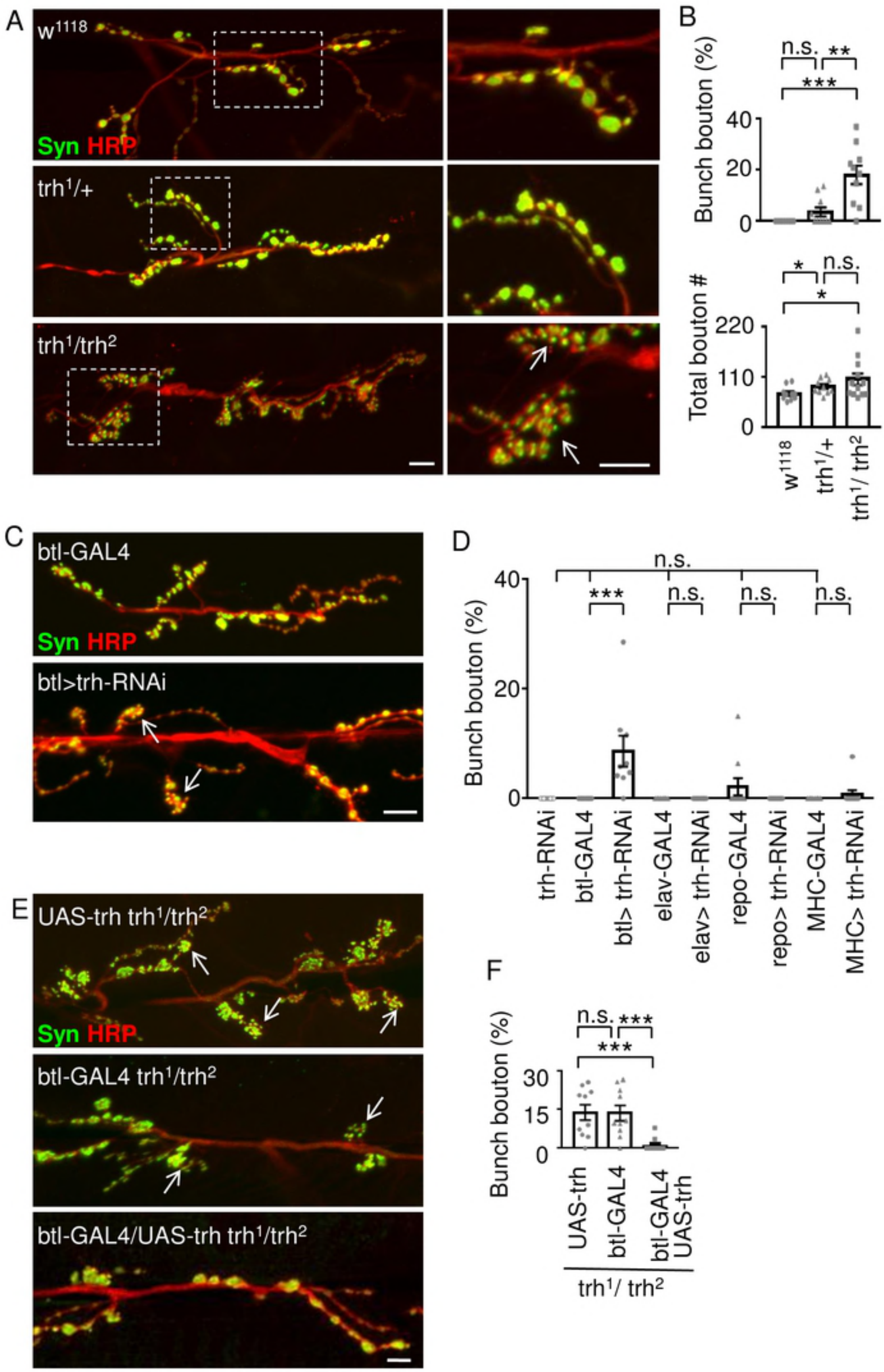
A
w1118
Syn HRP
trh1/+
trh1/trh2
B
Bunch bouton (%)
n.s.
**
***
40
20
0
Total bouton #
*
n.s.
*
220
110
0
w1118
trh1/+
trh1/ trh2
C
btl-GAL4
Syn HRP
btl>trh-RNAi
D
Bunch bouton (%)
n.s.
***
n.s.
n.s.
n.s.
40
20
0
trh-RNAi
btl-GAL4
btl> trh-RNAi
elav-GAL4
elav> trh-RNAi
repo-GAL4
repo> trh-RNAi
MHC-GAL4
MHC> trh-RNAi
E
UAS-trh trh1/trh2
Syn HRP
btl-GAL4 trh1/trh2
btl-GAL4/UAS-trh trh1/trh2
F
Bunch bouton (%)
n.s.
***
***
30
15
0
UAS-trh
btl-GAL4
btl-GAL4 UAS-trh
trh1/ trh2

Figure